

Performance Analysis of Radiometric Autonomous Navigation for Lunar Satellite Network Topologies

Turan, E.; Speretta, S.; Gill, E.K.A.

Publication date

2022

Document Version

Final published version

Citation (APA)

Turan, E., Speretta, S., & Gill, E. K. A. (2022). *Performance Analysis of Radiometric Autonomous Navigation for Lunar Satellite Network Topologies*. 11th International Workshop on Satellite Constellations and Formation Flying, Milan, Italy.

Important note

To cite this publication, please use the final published version (if applicable). Please check the document version above.

Copyright

Other than for strictly personal use, it is not permitted to download, forward or distribute the text or part of it, without the consent of the author(s) and/or copyright holder(s), unless the work is under an open content license such as Creative Commons.

Takedown policy

Please contact us and provide details if you believe this document breaches copyrights. We will remove access to the work immediately and investigate your claim.

PERFORMANCE ANALYSIS OF RADIOMETRIC AUTONOMOUS NAVIGATION FOR LUNAR SATELLITE NETWORK TOPOLOGIES

Erdem Turan*, Stefano Speretta[†] and Eberhard Gill[‡]

This study provides a performance analysis of radiometric autonomous navigation for the lunar satellite network topologies formed by three spacecraft at various orbits. This work is built on the Linked Autonomous Interplanetary Satellite Orbit Navigation (LiAISON) method and uses mesh (distributed) and centralized (star) network topologies. The optimal interlink network topologies and Distributed Satellite Systems (DSS) geometry have been investigated based on the Circular-Restricted Three-Body problem (CRTBP) and the Extended Kalman Filter (EKF) for state estimation. The network topologies consisted of all the possible combinations of 16 spacecraft at various L_1/L_2 Halo, Lyapunov, and Lunar orbits. It has been shown that the autonomous navigation system provided better state estimation results for the mesh topology than for the centralized topology. Overall, the lunar satellite network topologies consisting of orbits with large inter-satellite link distances and short orbital periods would benefit most from the radiometric autonomous navigation.

keywords: autonomy, navigation, topology, mesh, centralized,

1. Introduction

During the past years, small satellites have obtained great attention, also for lunar missions. One of the reasons are the advances in satellite technology resulting into a reduction in size and cost of the satellites. In addition, increasing piggyback opportunities will provide more frequent launch opportunities to the lunar vicinity. These missions form almost 40% of all the planned deep space small satellite missions [1] proposed by universities, space agencies, and others [2–6]. In these missions, the proposed orbit determination (OD) approach is, in general, ground-based radiometric tracking. However, this approach could be expensive while small satellite developments aim at low-cost. Autonomous OD, on the other hand, could provide a cost reduction, increased performance, and/or increased reliability. There are also missions that could not be possible without autonomy such as rendezvous missions.

Up to now, different autonomous orbit determination methods have been studied and implemented. One of them, Linked Autonomous Interplanetary Satellite Orbit Navigation (LiAISON) [7–9], uses solely inter-satellite observations to estimate the absolute states of the involved satellites when at least one of them has an orbit with a unique size, shape, and

orientation. Until now, studies have presented the capabilities of LiAISON in lunar and deep space missions [7, 9–14].

Distributed Satellite Systems (DSS), such as formations or constellations, on the other hand, provide opportunities to achieve mission goals working with multiple spacecraft (S/C). Considering small satellite missions involving DSS in the lunar vicinity, one-hop link configuration via a mother-craft are the baseline communications approach to transfer payload data to the ground. This centralized or star topology is thus the preferred configuration for communication. However, additional links between the different daughter-craft could be beneficial for missions involving multiple S/C. The mesh or distributed topology provides interactions between all S/C, and its performance thus is not dependent on the centralized node (mother-craft). These topologies could benefit from the LiAISON OD method using the existing communication links between them. In case the OD process is performed for more than two S/C in the DSS, there are topics that have not yet been theoretically investigated such as optimal interlink network topology and DSS geometry. This study aims at providing a performance analysis for radiometric autonomous navigation for lunar satellite network topologies formed by three S/C at various orbits taking advantage of the best orbital geometries. This might ease the geometrical problems of the ground-based navigation in the Earth-Moon system. It is expected that a mesh (distributed) topology would provide better overall OD performance than a star (centralized) topology,

*Space Systems Engineering, Delft University of Technology, The Netherlands, e.turan@tudelft.nl

[†]Space Systems Engineering, Delft University of Technology, The Netherlands, s.speretta@tudelft.nl

[‡]Space Systems Engineering, Delft University of Technology, The Netherlands, E.K.A.Gill@tudelft.nl

due to an additional links providing extra information to the navigation filter. However, a study needs to be performed on how much improvement could actually be obtained. In addition, OD performance would vary even in the same relative geometry between S/C due to selected mother-craft (centralized node) configuration in the star topology. It is crucial to decide which S/C in the star topology would collect the observations and perform on-board navigation. This research aims to also provide decision support for the problem.

In the following sections, at first, autonomous radiometric navigation is presented and then, network topologies are discussed. Orbit determination models are introduced including dynamical, measurement, and estimation models. After that, the navigation simulation setup and results are presented. Finally, conclusions are drawn.

2. Autonomous Radiometric Navigation

This study investigates the LiAISON OD performances for the network topologies at the lunar vicinity. Autonomous OD requires absolute state estimation without using any ground-based measurement. Basically, in this application, satellite-to-satellite observations must provide the absolute position and velocity estimation and these states must be observable from the available measurements. In the two-body problem, inter-satellite measurements do not provide the estimation for the absolute orientation of the orbital planes and only the relative orientation can be observed. However, in an asymmetrical gravity field, it is possible to achieve full states estimation via satellite-to-satellite tracking. The LiAISON method uses only inter-satellite measurements to estimate the absolute S/C states if one of the S/C has an orbit with unique size, shape, and orientation. The LiAISON performance depends on various factors, such as observation type, accuracy, precision, frequency, the relative geometry between satellites, and others. In general, LiAISON would provide better OD performance for two-S/C configurations if satellites have high elliptical non-coplanar orbits with large separation, and short-periodic orbits [7,8,11,15]. Range observations provide better state estimations than the range-rate for such application [7,14]. Systematic biases affect the performance specifically [7]. LiAISON would still provide acceptable state estimation for missions with high inter-satellite measurement errors (in the order of 100 m 1σ ranging error) at the lunar vicinity [14].

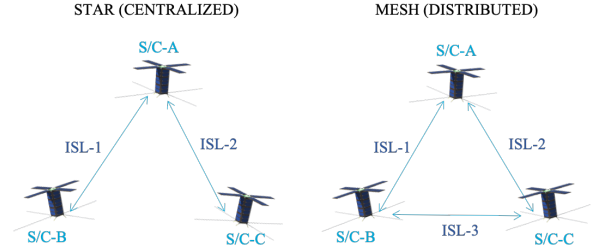


Fig. 1: Representation of centralized and mesh network topologies for the three S/C case

3. Network Topologies

There are different communication topologies for S/C formations including star (centralized), mesh (distributed), or hierarchical (hybrid) topology. Star or centralized topologies have a chief S/C node and deputies in the formation. The communication link is only between the chief and deputies while in the mesh or distributed topology, the communication link is between all nodes. The hierarchical or hybrid topology, on the other hand, has multiple layers and consists of two or more star networks. Because this study focused on the three S/C case only, the hierarchical topology has not been investigated. A schematic representation of centralized and mesh topologies can be seen in Figure 1.

The centralized topology, as compared to the mesh one, has a simpler design. However, the network relies on the performance of the mother-craft (central node) and any failure on the central node may influence the mission significantly [16]. On the other hand, the mesh topology has the advantage of direct interactions between all S/C and the network is not affected by communication failures as much as the centralized one. However, complexity increases as the number of S/C in the topology increases (considering for N spacecraft, $N - 1$ versus $N(N - 1)/2$ connections in the centralized and mesh topologies, respectively).

4. Orbit Determination Models

This section presents the orbit determination models and the performance analysis methods used in this paper. The dynamical, measurement and estimation models and the observability aspects will be presented in the following subsections.

4.1 Dynamical Model

In this study, the dynamical model is formulated as Circular Restricted Three-body Problem (CRTBP). This assumes that there are two massive bodies, Earth (P_1 , with mass m_1) and Moon (P_2 with mass m_2), moving under their mutual gravitational force in a circular orbit around each other with a radius r_{12} . A third body of mass m_3 with $m_3 \ll m_1$ and $m_3 \ll m_2$, cannot impact the motion of primary bodies, P_1 and P_2 . A co-moving reference frame is also used with its origin at the barycenter of the two bodies, the positive x -axis pointing from the barycenter to P_2 , the positive y -axis to the P_2 velocity vector, and the z -axis being perpendicular to the orbital plane. The equations of motion for the CRTBP are [7]:

$$\ddot{x} = 2\dot{y} + x - (1 - \mu)\frac{x + \mu}{r_1^3} - \mu\frac{x + \mu - 1}{r_2^3} \quad [1]$$

$$\ddot{y} = (1 - \frac{1 - \mu}{r_1^3} - \frac{\mu}{r_2^3})y - 2\dot{x} \quad [2]$$

$$\ddot{z} = (\frac{\mu - 1}{r_1^3} - \frac{\mu}{r_2^3})z \quad [3]$$

where

$$r_1 = \sqrt{(x + \mu)^2 + y^2 + z^2}$$

$$r_2 = \sqrt{(x + \mu - 1)^2 + y^2 + z^2}$$

For the Earth-Moon system, the gravitational parameter μ is 0.01215, the normalized time t^* 4.343 days, and the normalized length l^* 384 747.96 km, respectively.

4.2 Measurement Model

In this study, inter-satellite observables are collected via two-way radiometric measurements. The pseudorange has been used in the measurement model. Regarding the estimated states, parameters are a 18-dimensional position and velocity vector representing all three S/C dynamical states.

$$\mathbf{X} = (\mathbf{r}_1, \mathbf{v}_1, \mathbf{r}_2, \mathbf{v}_2, \mathbf{r}_3, \mathbf{v}_3)^T \quad [4]$$

where subscript represents the S/C number.

The measurement model consists of the geometric distance between S/C, overall clock error, bias, and other error sources. The geometric range is given as follows:

$$R = \frac{1}{2} c(t_4 - t_1) + \Delta\rho \quad [5]$$

By ignoring the light-time correction, and by assuming the speed of light is greater than the S/C relative

velocity, $c \gg v$, the geometric range can be modeled as:

$$R = \sqrt{(x_1 - x_2)^2 + (y_1 - y_2)^2 + (z_1 - z_2)^2} \quad [6]$$

where x_i, y_i and z_i represents the position components of S/C, $i = 1, 2, 3$, states and the pseudorange observations can be modeled as:

$$\rho = R + c(\psi_{t_4} - \psi_{t_1}) + c(\Delta_{tx} + \Delta_{rx}) + c\Delta_{trx} + \rho_{\text{noise}} \quad [7]$$

$$\rho = \sqrt{(\mathbf{r}_1 - \mathbf{r}_2) \cdot (\mathbf{r}_1 - \mathbf{r}_2)} + \rho_{\text{bias}} + \rho_{\text{noise}} \quad [8]$$

where ψ_{t_4} and ψ_{t_1} are the clock states at t_4 and t_1 respectively. The transponder transmit and receive line delays are Δ_{tx} and Δ_{rx} , respectively and Δ_{trx} is the line delay on the S/C transponding the ranging signal. All these terms are combined as ρ_{bias} and ρ_{noise} representing the un-modelled statistical error sources. In case inter-satellite tracking is done based on a conventional Pseudo-Noise (PN) ranging method and considering a non-coherent transponder with a PN square wave shaped ranging signal, and a chip tracking loop, the following one-way ranging error (1σ) would be observed [17]:

$$\sigma_{\rho_{PN}} = \frac{c}{8f_{rc}} \sqrt{\frac{B_L}{(P_{RC}/N_0)}} \quad [9]$$

where f_{rc} the frequency of the ranging clock component, B_L one-sided loop noise bandwidth, P_{RC} power of the ranging clock component, and N_0 one-side noise power spectral density.

4.3 Estimation Model

This study uses the Extended Kalman Filter (EKF) as an estimation model. Given the initial state \mathbf{X}_0 and state covariance \mathbf{P}_0 at the initial time, the EKF processes the inter-satellite range observations at measurement epochs. The EKF consists of a prediction and a correction step:

$$\dot{\mathbf{X}} = \mathbf{f}(\mathbf{X}, t), \quad \mathbf{X}(t_{k-1}) = \hat{\mathbf{X}}_{k-1} \quad [10]$$

$$\bar{\mathbf{P}}_k = \Phi(t_k, t_{k-1})\mathbf{P}_{k-1}\Phi^T(t_k, t_{k-1}) + \mathbf{Q} \quad [11]$$

where $\Phi(t_k, t_{k-1})$ is the state transition matrix from t_{k-1} to t_k and \mathbf{Q} is the process noise matrix. The correction step is:

$$\mathbf{K}_k = \bar{\mathbf{P}}_k \tilde{\mathbf{H}}_k^T [\tilde{\mathbf{H}}_k \bar{\mathbf{P}}_k \tilde{\mathbf{H}}_k^T + \mathbf{W}_k]^{-1} \quad [12]$$

$$\hat{\mathbf{X}}_k = \mathbf{X}_k + \mathbf{K}_k [\mathbf{y}_k - \tilde{\mathbf{H}}_k \mathbf{X}_k] \quad [13]$$

$$\mathbf{P}_k = [\mathbf{I} - \mathbf{K}_k \tilde{\mathbf{H}}_k] \bar{\mathbf{P}}_k \quad [14]$$

where $\hat{\mathbf{X}}$ is the state estimate, \mathbf{K} is the Kalman gain, $\tilde{\mathbf{H}}$ is the measurement sensitivity, \mathbf{P} is the error covariance estimate, and \mathbf{W} is the state noise compensation matrix.

4.4 Observability

The observability analysis is used to relate OD performance and the relative geometry between S/C. It is also used for other aspects such as observation data, accuracy, frequency, etc. The degree of the system observability is evaluated via the observability Gramian as follows:

$$\mathbf{N} = \sum_{k=1}^l \Phi(t_k, t_0)^T \tilde{\mathbf{H}}_k^T \tilde{\mathbf{H}}_k \Phi(t_k, t_0) \quad [15]$$

In this study, two metrics are used for the observability assessment (by means of a Singular Value Decomposition (SVD)): the condition number, which is the ratio of the largest singular value to the smallest one, and unobservability index, which is the reciprocal of the smallest local singular value.

4.5 Performances Evaluation

In addition to the observability assessment, another performance analysis approach has been investigated. In [7], the largest axis of the 3D, 3σ error ellipsoid for the S/C at each timestep averaged over the entire fit span was used to evaluate the orbit estimation accuracy. The same approach has been implemented into this study as well, with the only difference being the usage of the EKF instead of a batch least squares implementation. The following equation is used to compute the length of the largest axis of the error ellipsoid [7]:

$$\beta_i = 3 \max(\sqrt{\lambda_j}) \quad [16]$$

where λ_j for $j = 1, 2, 3$ are the eigenvalues of $\mathbf{P}_{i3 \times 3}$ (representing position or velocity components of S/C) and the average value of the three spacecraft system

$$\bar{\beta} = \frac{1}{n} \sum_{i=1}^n \beta_i, \quad \beta_{ave} = \frac{1}{3} \sum_{j=1}^3 \bar{\beta}_j \quad [17]$$

where n is number of β values during the simulation. Because this study considers the topology consisted of three S/C, average value β_{ave} is calculated over their $\bar{\beta}$ values.

5. Navigation Simulations

This section presents the autonomous orbit determination results for the mesh and centralized mission

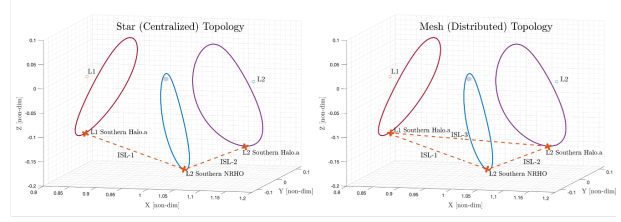


Fig. 2: Representation of centralized and mesh network topologies for the three S/C case

Table 1: Selected Lagrangian orbiters with their periods and Jacobi constants (Southern and northern Halo configurations have the same values)

Orbit	T (days)	C_j
L ₂ Halo a.	14.14	3.11
L ₂ Halo b.	13.77	3.09
L ₁ Halo a.	12.10	3.10
L ₁ Halo b.	11.98	3.08
L ₂ NRHO	6.87	3.04
L ₁ NRHO	7.83	3.00
L ₂ Lyapunov	18.72	3.10
L ₁ Lyapunov	18.81	3.11

scenarios. The simulation setup is given first, and thereafter results are presented.

5.1 Simulation setup

This study investigates the radiometric autonomous navigation performances for lunar satellite network topologies. For this purpose, the mesh and centralized topologies formed by three S/C have been studied. Basically, in the each mission scenario, the formation consists of three S/C. Depending on the network topology, the number of Inter-Satellite Link (ISL) has been set: two for the centralized topology or three for the mesh topology. A schematic representation of both topologies can be seen in Figure 2. This means that the navigation filter is fed by two different types of pseudorange measurements in the centralized topology and three different measurement types in the mesh topology.

This study considered various orbital setups for the lunar orbiters. In total, 16 different orbital setups have been investigated. These include, L₁/L₂ southern/northern Halo orbits, L₁/L₂ Lyapunov orbits, Lunar elliptical and polar-circular orbits. In order to see the effects of orbits at the same vicinity, two different non-coplanar L₁ and L₂ periodic Halo orbits have also been considered (a. and b.). It is known

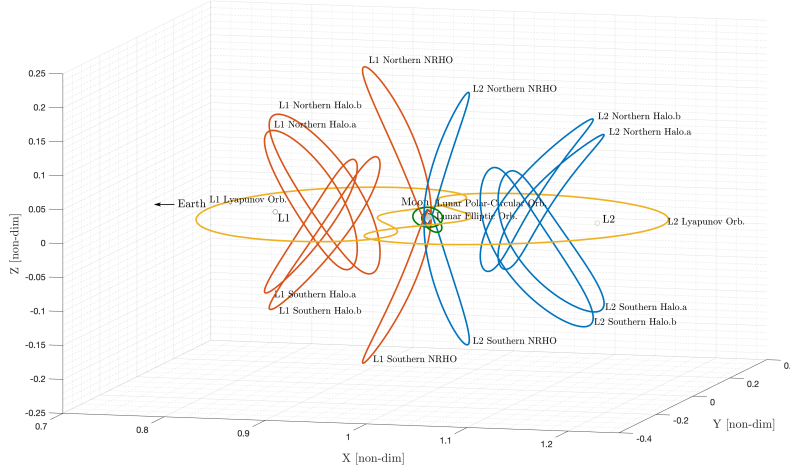


Fig. 3: Orbital trajectories considered in the study.

that coplanar orbits affect the observability of the system and thus the OD performance, so that this option has not been considered. All the trajectories can be seen in Figure 3. Regarding periodic Halos and Lyapunov orbits, their periods, T , and Jacobi energies, C_j , are given in Table 1. The Lunar elliptical orbit considered in this study has an inclination of 57 deg, a semi-major axis of 5735 km, and an eccentricity of 0.61. These are very similar orbital parameters of Lunar Pathfinder [18] which will be launched in the coming years, thus providing a realistic mission scenario for this study. In addition, a polar-circular orbit has been investigated with a 95 deg inclination and a 5735 km semi-major axis. Regarding the all different combinations, the mesh topology has a combination of N orbital configurations taken K at a time without repetition, $\binom{N}{K} = \frac{N!}{K!(N-K)!}$. In this case three S/C are taken and this gives $\binom{16}{3} = 560$ combinations for the mesh topology. In the centralized topology, as an extra, a central node should be selected from each S/C non-repetitive combinations (K -selection), so this results in a total number of $560 \times 3 = 1680$ combinations for the central topology.

The simulation duration is set to be 28 days (1.5 times the longest orbital period, 18.81 days, in the topology). About the inter-satellite range measurements, a 1σ error of 3 m (1 MHz f_{rc} , 25 dBHz P_{RC}/N_0 , 1 Hz B_L) has been assumed without any bias. It is known that measurement biases affect the OD performance. However, this study only investigates the geometrical relations and improvements with an additional inter-satellite link, so that measurement er-

Table 2: The diagonal state covariance \mathbf{P}_0 values and state errors (for the S/C numbers $i = 1, 2, 3$)

Parameter	Value
Position uncertainty, (x_i, y_i, z_i) , 1σ	1km
Velocity uncertainty, $(\dot{x}_i, \dot{y}_i, \dot{z}_i)$, 1σ	1cm/s
Initial position error, (x_i, y_i, z_i)	500 m
Initial velocity error, $(\dot{x}_i, \dot{y}_i, \dot{z}_i)$	1mm/s

rors were kept low and no bias was assumed. Note that, in this type application, the clock bias and drift can be estimated via inter-satellite measurements by extending the estimated state vector. However, this might affect the system observability, and thus the OD performance. The initial state \mathbf{X}_0 and diagonal state covariance \mathbf{P}_0 values can be found in Table 2.

5.2 Results

This section presents the simulation results starting from the centralized topology and then continuing with the mesh topology.

At first, an example scenario is given representing the centralized topology and its autonomous navigation performance. Basically, in this scenario, three S/C namely, L₁ southern Halo a., L₂ southern Near-Rectilinear Halo Orbit (NRHO), and L₂ southern Halo a., have been selected to illustrate the expected performance in this type of application (orbital trajectories can be seen in Figure 2). Estimation results are visible in Figure 4 showing that crosslink range measurements via the ISL between L₂ NRHO and

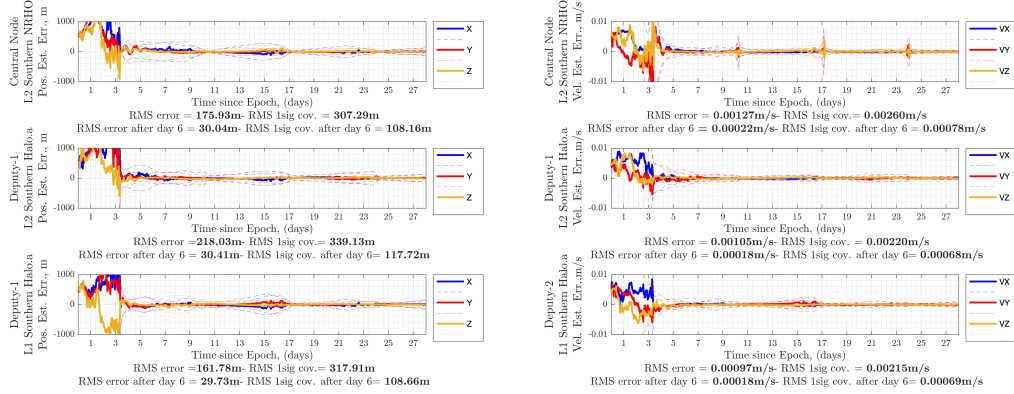


Fig. 4: The centralized topology state estimation (example scenario)

L_1 and L_2 Halos provide the position estimation uncertainty (1σ) below 150 m and velocity estimation uncertainty (1σ) below 8 mm/s for all S/C in the system after day 6. The positional states of NRHO can be estimated better when the S/C approaches the periselene. However, this is not valid for the velocity states. In general, 6 days since the initial epoch is sufficient to reach a stable estimation result. In this case, the condition number and the unobservability index are 9.82×10^{11} , 4.76×10^8 , respectively. This type of application requires the condition number to be less than 10^{16} for the problem to be observable [7]. $\beta_{ave-pos}$ and $\beta_{ave-vel}$ are 756 m and 5.44 mm/s, respectively. These values are, basically, representing the average values (over three S/C) of the highest 3σ uncertainty (position or velocity) during the simulation (including very first days of the simulation before the stable period).

Figure 5 and 6 represent the $\beta_{ave-pos}$ and $\beta_{ave-vel}$, respectively for all the combinations simulated in this study. As it can be seen, in general, the centralized topology combinations formed by either a lunar elliptical or polar-circular orbiters provides the best performances among all combinations. Combinations including the Lunar elliptical orbiter provide slightly better overall performances than the Lunar polar-circular orbiter (particularly for the velocity estimations). On the other hand, if the centralized topology is formed only by L_1 or L_2 Halos, it would give higher estimation errors. This is due to fact that orbital periods and relative positional changes in time are almost the same during the simulation. Basically, when S/C are in close proximity, certain directions are not well observable. In addition, the topology formed by both Lyapunov orbits didn't provide accu-

rate results (due to not positional change in z -axis) even if there is a high inter-satellite distance between them. It is not possible to show all the results considering the number of combinations, however, selected configurations can be seen in Table 3. In this table, T_{req} is also given representing the time required to reach 500 m overall 1σ position uncertainty. Basically, in the selected cases, the centralized topologies not formed by the Lunar orbiters couldn't reach that value within the simulation time (28 days). In brief, the best combinations would be formed by S/C with larger inter-satellite distances and higher differences in orbital periods. This would make the centralized topologies better performing if the topology is formed by Lunar orbiters and/or Halo orbiters at different Lagrangian points. An example would be a centralized topology formed by a Lunar elliptical, L_1 southern Halo and a L_2 northern Halo orbiters.

Regarding the mesh topology, state estimation results are better than for the centralized topology due to the additional link providing extra information to the navigation filter. Figure 7 represents the state estimation results for the mesh topology. Once again, the best performances have been achieved with the mesh topology formed by the Lunar orbiters. On the other hand, the formation formed only by L_1 or L_2 Halos couldn't provide the same performances. In Table 4, the selected mesh topologies can be seen. This time, in addition to other parameters, T_{req} has been improved and two cases have also reached the aimed 1σ uncertainty within 28 days. In general, there are slight performance improvements for the mesh topologies formed by the Lunar orbiters than the centralized topologies with the same geometries. In these cases, at minimum 10% performance improvement has been

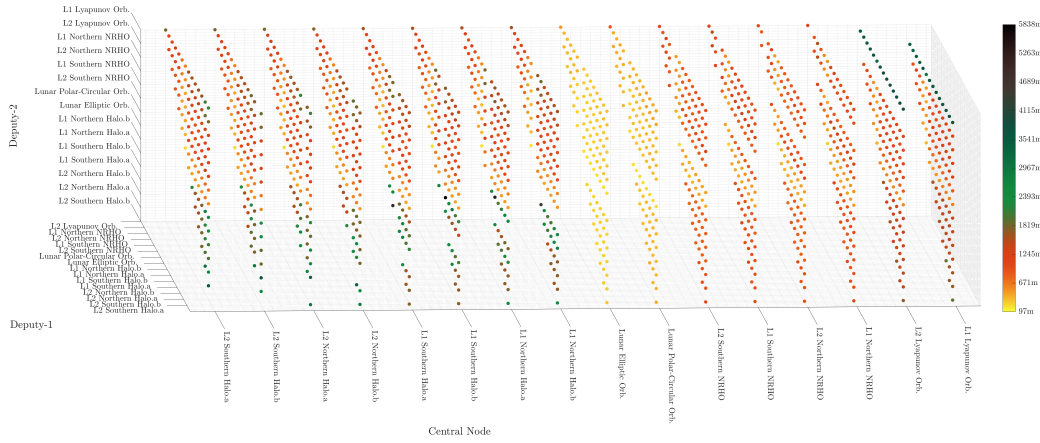
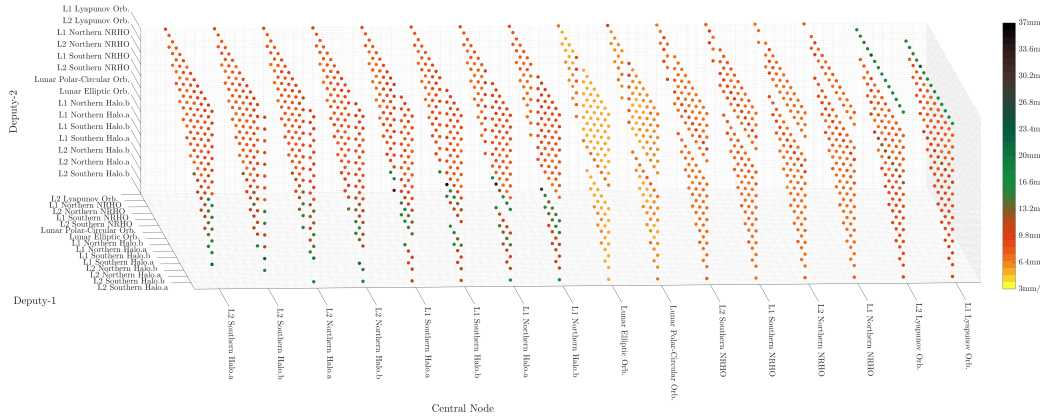

 Fig. 5: $\beta_{ave-pos}$ values for the centralized topology.

 Fig. 6: $\beta_{ave-vel}$ values for the centralized topology.

Table 3: Results for the selected centralized topologies.

Central Node	Deputy-1	Deputy-2	Cond.Num.	Unobs.Index	$\beta_{ave-pos}$ [m]	$\beta_{ave-vel}$ [mm/s]	T_{req} [days]
Lunar Elliptic Orb.	L2 Northern Halo.a	L1 Southern Halo.a	2.77×10^8	1.30×10^9	157	4.3	3.86
Lunar Polar-Circular Orb.	L2 Northern Halo.a	L1 Southern Halo.a	3.34×10^{10}	1.53×10^7	270	4.8	8.57
L1 Northern NRHO	L2 Northern Halo.a	L1 Southern Halo.a	6.58×10^{11}	3.14×10^8	786	5.1	-
L1 Lyapunov Orb.	L2 Southern Halo.b	L1 Northern NRHO	1.01×10^{12}	4.86×10^8	1146	6.8	-
L2 Northern Halo.b	L1 Northern Halo.a	L1 Northern Halo.b	1.34×10^{14}	5.48×10^{10}	1480	9.6	-
L2 Southern Halo.b	L2 Northern Halo.a	L2 Northern Halo.b	1.92×10^{14}	5.22×10^{10}	2949	17.3	-

Table 4: Results for the selected mesh topologies.

1st S/C	2nd S/C	3rd S/C	Cond.Num.	Unobs.Index	$\beta_{ave-pos}$ [m]	$\beta_{ave-vel}$ [mm/s]	T_{req} [days]
L2 Northern Halo.a	L1 Southern Halo.a	Lunar Elliptic Orb.	3.11×10^8	1.30×10^9	139	3.4	3.06
L2 Northern Halo.a	L1 Southern Halo.a	Lunar Polar-Circular Orb.	3.67×10^{10}	1.53×10^7	244	4.4	7.46
L2 Northern Halo.a	L1 Southern Halo.a	L1 Northern NRHO	8.27×10^{11}	3.12×10^8	599	3.8	22.21
L2 Southern Halo.b	L1 Northern NRHO	L1 Lyapunov Orb.	8.88×10^{11}	3.42×10^8	614	3.9	23.51
L2 Northern Halo.b	L1 Northern Halo.a	L1 Northern Halo.b	8.22×10^{13}	3.22×10^{10}	1026	6.3	-
L2 Southern Halo.b	L2 Northern Halo.a	L2 Northern Halo.b	9.96×10^{13}	2.69×10^{10}	1672	9.1	-

- Y. Kawakatsu, T. Ikenaga, K. Oguri, and K. Oshima. Mission analysis for the EM-1 CubeSats EQUULEUS and OMOTENASHI. *IEEE Aerospace and Electronic Systems Magazine*, 34(4):38–44, apr 2019.
- [4] B. K. Malphrus, K. Z. Brown, J. Garcia, C. Conner, J. Kruth, M. S. Combs, N. Fite, S. McNeil, S. Wilczweski, K. Haught, A. Zucherman, P. Clark, K. Angkasa, N. Richard, T. Hurford, D. Folta, C. Brambora, R. MacDowall, P. Mason, S. Hur-Diaz, J. Breeden, R. Nakamura, A. Martinez, and M. M. Tsay. The lunar Ice-Cube EM-1 mission: Prospecting the moon for water ice. *IEEE Aerospace and Electronic Systems Magazine*, 34(4):6–14, apr 2019.
- [5] T. Hashimoto, T. Yamada, M. Otsuki, T. Yoshimitsu, A. Tomiki, W. Torii, H. Toyota, J. Kikuchi, N. Morishita, Y. Kobayashi, T. Ito, H. Tanno, A. Nagamatsu, and H. Morimoto. Nano semihard moon lander: OMOTENASHI. *IEEE Aerospace and Electronic Systems Magazine*, 34(9):20–30, sep 2019.
- [6] C. Hardgrove, R. Starr, I. Lazbin, A. Babuscia, B. Roebuck, J. DuBois, N. Struebel, A. Colaprete, D. Drake, E. Johnson, J. Christian, L. Heffern, S. Stem, S. Parlapiano, M. Wiens, A. Genova, D. Dunham, D. Nelson, B. Williams, J. Bauman, P. Hailey, T. OBrien, K. Marwah, L. Vlieger, J. Bell, T. Prettyman, T. Crain, E. Cisneros, N. Cluff, G. Stoddard, and M. Kaffine. The lunar polar hydrogen mapper CubeSat mission. *IEEE Aerospace and Electronic Systems Magazine*, 35(3):54–69, mar 2020.
- [7] K. A. Hill. *Autonomous Navigation in Libration Point Orbits*. PhD thesis, University of Colorado, 2007.
- [8] K. Hill and G. H. Born. Autonomous interplanetary orbit determination using satellite-to-satellite tracking. *Journal of Guidance, Control, and Dynamics*, 30(3):679–686, may 2007.
- [9] K. A. Hill and G. H. Born. Autonomous orbit determination from lunar halo orbits using crosslink range. *Journal of Spacecraft and Rockets*, 45(3):548–553, may 2008.
- [10] J. Leonard, B. Jones, E. Villalba, and G. Born. Absolute orbit determination and gravity field recovery for 433 eros using satellite-to-satellite tracking. In *AIAA/AAS Astrodynamics Specialist Conference*. American Institute of Aeronautics and Astronautics, aug 2012.
- [11] W. Wang, L. Shu, J. Liu, and Y. Gao. Joint navigation performance of distant retrograde orbits and cislunar orbits via LiAISON considering dynamic and clock model errors. *Navigation*, 66(4):781–802, dec 2019.
- [12] J. M. Leonard. *Supporting Crewed Missions using LiAISON Navigation in the Earth-Moon System*. PhD thesis, University of Colorado, 2015.
- [13] Kohei Fujimoto, Nathan Stacey, and James M. Turner. Stereoscopic image velocimetry as a measurement type for autonomous asteroid gravimetry. In *AIAA/AAS Astrodynamics Specialist Conference*. American Institute of Aeronautics and Astronautics, Sep 2016.
- [14] E. Turan, S. Speretta, and E. Gill. Autonomous navigation performance of cislunar orbits considering high crosslink measurement errors. In *2022 IEEE Aerospace Conference*, pages 1–11, 2022.
- [15] T. Qin, D. Qiao, and M. Macdonald. Relative orbit determination using only intersatellite range measurements. *Journal of Guidance, Control, and Dynamics*, 42(3):703–710, 2019.
- [16] R. Sun. *Relative Navigation for Satellite Formation Flying based on Radio Frequency Metrology*. PhD thesis, Delft University of Technology, 2014.
- [17] CCSDS. Pseudo-noise (pn) ranging systems. February 2014.
- [18] M. Scotti, C. Botteron, M. Rico, F. Basile, V. Massaras, B. Kieniewicz, J. Svatoň, P. Giordano, and J. Ventura-Traveset. Navimoon – ultra-high sensitivity gnss receiver for lunar navigation. In *NAVITEC 2022*, April 2022.